

Oxygen Fugacity Evolution of the Mantle Lithosphere Beneath the North China Craton

Ji-Feng Ying¹, Chen-Yang Ye¹, Yanjie Tang², XinMiao Zhao³, and Hongfu Zhang⁴

¹State Key Laboratory of Lithospheric Evolution, Institute of Geology and Geophysics, Chinese Academy of Sciences

²Institute of Geology and Geophysics, Chinese Academy of Sciences

³Institute of Geology and Geophysics, Chinese Academy of Sciences

⁴institute of geology and geophysics, CAS

November 22, 2022

Abstract

Oxygen fugacity controls the behavior of multivalent elements and compositions of C-O-H fluids in Earth's mantle, which further affects the cycling of materials between the deep interior and surface of Earth. The redox state of mantle lithosphere of typical stable cratons has been well documented, but how oxygen fugacity had varied during craton destruction remains unclear. This study estimates the oxygen fugacity of peridotite xenoliths entrained in Mesozoic and Cenozoic basalts on North China Craton (NCC), a typical destroyed craton. The results reveal that the mantle lithosphere beneath the NCC experienced three stages of evolution in terms of oxygen fugacity. First, the refractory and oxidized peridotite xenoliths indicate the lithospheric mantle experienced a high degree of melt extraction and later long-term and complicated metasomatism before craton destruction. Then, the variations of olivine Mg-number in peridotites and oxygen fugacity reveal significant metasomatism by melts originated from the shallow asthenosphere during the destruction of the NCC since the Mesozoic. The third stage may have occurred when mantle peridotites interacted with silica-undersaturated melts stemmed from the mantle transition zone where the stagnant Pacific slab underlies. This study further verifies that the asthenospheric convection induced by the roll-back of the subducted paleo-Pacific slab played a crucial role in the destruction of the NCC and helps understand the oxygen fugacity variability during the later life of the craton.

1 **Oxygen Fugacity Evolution of the Mantle Lithosphere Beneath the North China**
2 **Craton**

3 **Chen-Yang Ye^{1,2}, Ji-Feng Ying^{1,2,3*}, Yan-Jie Tang^{1,2,3}, Xin-Miao Zhao^{1,3}, Hong-Fu**
4 **Zhang^{1,2,3}**

5 ¹ State Key Laboratory of Lithospheric Evolution, Institute of Geology and Geophysics, Chinese
6 Academy of Sciences, Beijing 100029, China

7 ² College of Earth and Planetary Sciences, University of Chinese Academy of Sciences, Beijing
8 100049, China

9 ³ Innovation Academy for Earth Science, Chinese Academy of Sciences, Beijing 100029, China

10 * Corresponding author: Ji-Feng Ying (email: jfyang@mail.iggcas.ac.cn)

11 ORCID iD: <https://orcid.org/0000-0002-1013-8009>

12

13 **Key Words:** Oxygen fugacity, Peridotite, Lithospheric mantle, Metasomatism, North China
14 Craton.

15

16 **Key Points:**

17 ● Peridotite xenoliths in Meso-Cenozoic basalts from the North China Craton fall into four
18 groups and record different oxygen fugacities

19 ● The oxygen fugacity variability of the peridotites results from mantle processes
20 associated with the destruction of the North China Craton

21

22 Abstract

23 Oxygen fugacity controls the behavior of multivalent elements and compositions of C-O-H fluids
24 in Earth's mantle, which further affects the cycling of materials between the deep interior and
25 surface of Earth. The redox state of mantle lithosphere of typical stable cratons has been well
26 documented, but how oxygen fugacity had varied during craton destruction remains unclear. This
27 study estimates the oxygen fugacity of peridotite xenoliths entrained in Mesozoic and Cenozoic
28 basalts on North China Craton (NCC), a typical destroyed craton. The results reveal that the
29 mantle lithosphere beneath the NCC experienced three stages of evolution in terms of oxygen
30 fugacity. First, the refractory and oxidized peridotite xenoliths indicate the lithospheric mantle
31 experienced a high degree of melt extraction and later long-term and complicated metasomatism
32 before craton destruction. Then, the variations of olivine Mg-number in peridotites and oxygen
33 fugacity reveal significant metasomatism by melts originated from the shallow asthenosphere
34 during the destruction of the NCC since the Mesozoic. The third stage may have occurred when
35 mantle peridotites interacted with silica-undersaturated melts stemmed from the mantle transition
36 zone where the stagnant Pacific slab underlies. This study further verifies that the asthenospheric
37 convection induced by the roll-back of the subducted paleo-Pacific slab played a crucial role in
38 the destruction of the NCC and helps understand the oxygen fugacity variability during the later
39 life of the craton.

40 Plain Language Summary

41 The sub-continental lithospheric mantle is one of the most important reservoirs of carbon. Thus
42 its oxygen fugacity controls the stability of diamond and the compositions of C-O-H fluids.
43 Previous studies have revealed how the oxygen fugacity changes with depth in the upper mantle
44 beneath stable craton. However, cratons are not forever and capable of being destroyed and the
45 North China Craton is one of the most typical destructed cratons globally, as evidenced by
46 extensive magmatism and tectonic deformation since the Mesozoic. The variation of oxygen
47 fugacity during the destruction of the craton, as yet, remains unclear. We estimated the oxygen
48 fugacity of peridotite xenoliths in Mesozoic and Cenozoic basalts on the North China Craton to
49 solve this problem. The oxygen fugacities of the xenoliths record the three-stage evolution of the
50 mantle lithosphere. The evolution process involves complicated secular oxidation before the
51 craton destruction, the widespread reduction by asthenosphere-derived melts, and more oxidized

52 metasomatism by melts derived from the mantle transition zone, where the subducted Pacific
53 plate is stagnant.

54 **1 Introduction**

55 Oxygen fugacity (f_{O_2}) is a critical parameter that controls the oxidation state of multi-valence
56 elements, such as vanadium, carbon, and iron. (Frost & McCammon, 2008). The variation of f_{O_2}
57 affects the species of C-O-H bearing fluids and melts, which in turn change the solidus and the
58 nature of derived melts (Foley, 2011). For example, as a typical igneous rock that outcropped in
59 stable craton, volatile-rich kimberlites, are generally believed to be the product of interaction
60 between CO_2 and deep upper mantle under an oxidized condition (Sun & Dasgupta, 2020).

61 However, diamond-bearing xenoliths captured by kimberlites imply a reduced background in the
62 lithospheric mantle of the stable craton (Lazarov et al., 2009; McCammon & Kopylova, 2004).

63 Based on kimberlite-borne peridotite xenoliths, previous studies have established a P- $\log f_{O_2}$
64 profile of stable craton lithospheric mantle (e.g., Creighton et al., 2010; Goncharov et al., 2012;
65 Lazarov et al., 2009). On the one hand, the oxygen fugacity decreases with increasing pressure,
66 proving that diamond is stable in the lower lithospheric mantle (e.g., Creighton et al., 2010;
67 Goncharov et al., 2012; Lazarov et al., 2009). On the other hand, the oxygen fugacity of the
68 stable craton is higher than the ambient asthenosphere, suggesting that oxidized metasomatism
69 may have also influenced the stable craton (Creighton et al., 2009; Foley, 2011).

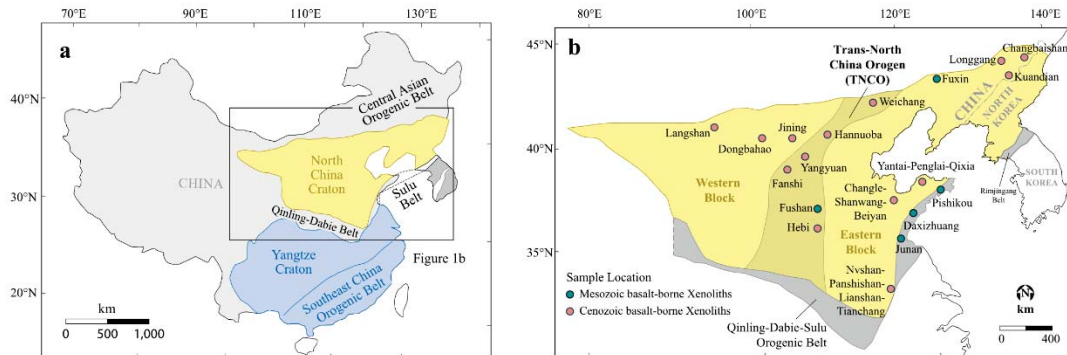
70 However, cratons are not forever and capable of being destroyed. The North China craton (NCC)
71 is one of the typical destroyed cratons, as evidenced by extensive magmatism, deformation, and
72 metamorphic core complex during Meso-Cenozoic (Wu et al., 2019). Although numerous studies
73 have been carried out to understand this catastrophic change, the exact cause and detailed
74 mechanism leading to the craton destruction is still hotly debated. Primarily, few investigations
75 are from a perspective of mantle redox state. So, it is valuable to figure out the redox state of the
76 upper mantle beneath the NCC at different geological times, how oxygen fugacity varied and
77 clues that f_{O_2} of peridotite xenoliths bears to unravel the geological processes during the craton
78 destruction.

79 This paper collects numerous published geochemical data of peridotite xenoliths entrained in
80 Mesozoic and Cenozoic basalts on North China Craton (NCC) and estimates their oxygen

81 fugacity. The yielded data reveal the redox state of the mantle lithosphere beneath the NCC and
 82 how it has changed during the craton destruction and factors affecting such variations.

83 2 Geological Setting

84 The NCC is one of the oldest cratons in the world with Archean crustal remnants as old as 3.8 Ga
 85 (Liu et al., 1992). It can be divided into the Eastern Block, the Trans-North China Orogen
 86 (TNCO), and the Western Block based on geology, tectonic evolution, and P–T–t paths of
 87 metamorphic basement rocks (Figure 1) (Zhao et al., 2005). It is generally reckoned that the
 88 Eastern and Western blocks evolved independently from late Archean to early Paleoproterozoic
 89 times before colliding into a coherent craton and final cratonization along the Trans-North China
 90 Orogen belt at ca. 1.85 Ga (Zhao et al., 2005). Since then, the NCC had essentially remained
 91 stable until the Mesozoic.



92
 93 **Figure 1.** (a) Tectonic subdivision of the Chinese continent and the location of the NCC
 94 (modified after Wu et al., 2019). (b) Schematic geological map of the NCC, showing the three-
 95 fold tectonic subdivision (modified after Wu et al., 2019) and the localities of peridotites
 96 xenoliths entrained by Mesozoic and Cenozoic mafic rocks.

97 Since the Mesozoic, deformation and extensive magmatism triggered by circum-craton
 98 subduction suggest the NCC, except the Western Block, has lost its stability (Wu et al., 2019).
 99 From the view of peridotite xenoliths, the thick refractory lithospheric keel was removed and
 100 replaced by fertile peridotites (Zheng et al., 2012). Meanwhile, the geotherm of the lithosphere
 101 underneath the eastern part of the NCC soared from 40 mW/m² in Paleozoic to >80 mW/m² in
 102 Mesozoic (Menzies & Xu, 1998). Likewise, geophysical imaging verifies that the thickness of
 103 the lithosphere of the Eastern Block is drastically thinned to about 70–80 km from greater than

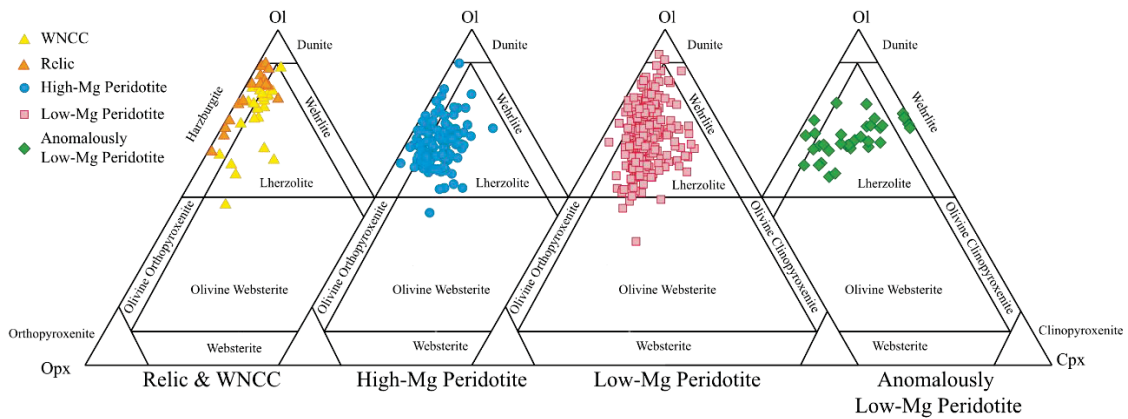
104 200 km in Paleozoic. In contrast, the Western Block keeps almost intact (Chen et al., 2009).
105 Accompanied by the NCC destruction are the widespread Meso-Cenozoic basaltic rocks,
106 especially in the Eastern Block and the TNCO, which captured a large amount of mantle
107 peridotite xenoliths. Previous investigations on these xenoliths have yielded an enormous amount
108 of geochemical data, making it possible to draw a whole picture of the redox state of the mantle
109 lithosphere beneath the NCC.

110 **3 Data, or a descriptive heading about data**

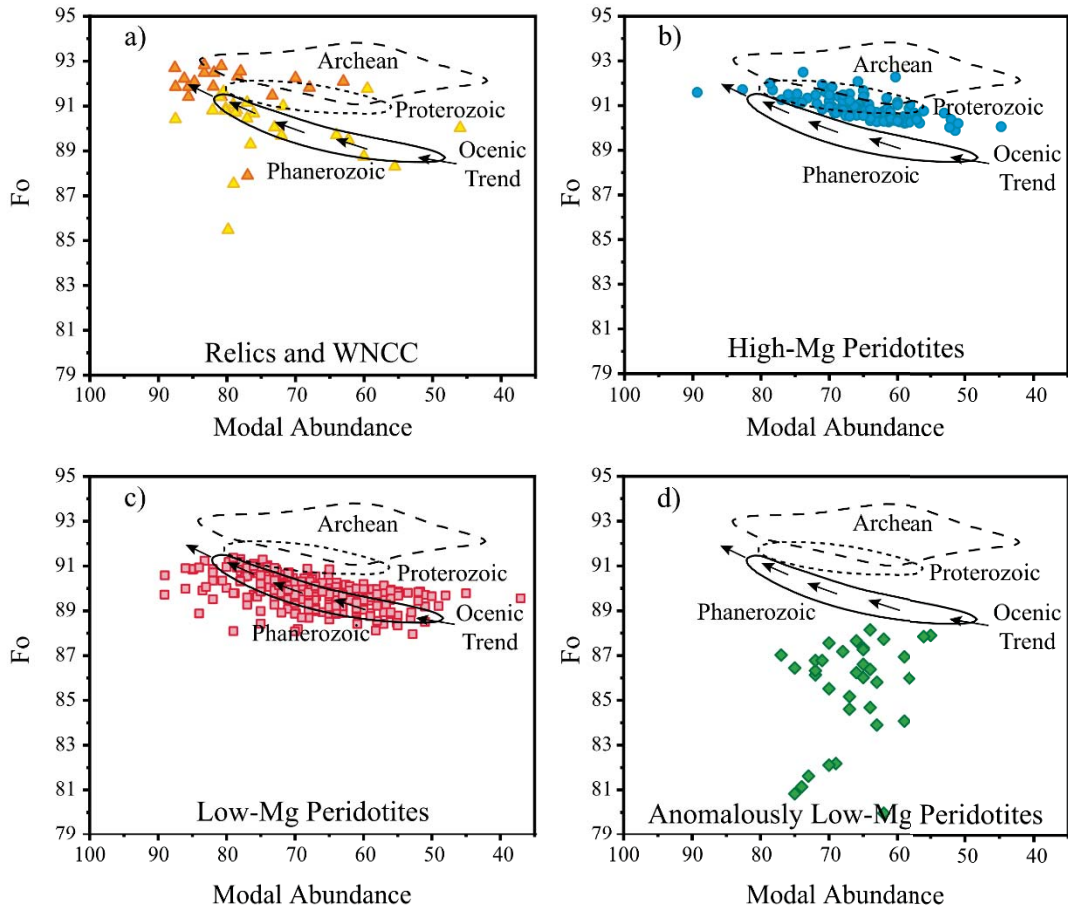
111 Thanks to previous studies, ample mineral compositions of peridotite xenoliths entrained in both
112 Mesozoic and Cenozoic basalts are available to date, which gives us an excellent chance to do
113 the research comprehensively. All the available peridotite xenoliths captured by basalts of
114 different ages and locations are all compiled in Figure 1. After collecting 605 peridotite
115 xenoliths, we estimate each sample's equilibrium temperature and oxygen fugacity before
116 performing subsequent statistical analysis. The reference of each sample is listed in Text S1.

117 The abovementioned peridotite xenoliths are mainly harzburgite and lherzolite, with a few
118 amounts of wehrlite (Figure 2). We divide them into four groups based on the modal abundance
119 and the Mg-number of olivine. The first group consists of Fushan, Hebi, and other localities from
120 the Western Block of the NCC. The first group consists of Fushan, Hebi, and other localities
121 from the Western Block of the NCC. The first-group xenoliths likely represent the relics of the
122 Archean mantle due to their high olivine modal abundance and Mg-number (Figure 3a), and the
123 Archean ages revealed by osmium isotope (Liu et al., 2011; Xu et al., 2010; Zheng et al., 2001).
124 Geophysical imaging has demonstrated that the lithosphere of the Western Block underwent
125 insignificant thinning (Chen et al., 2009). Therefore, peridotites xenoliths from the Western
126 Block can also represent the ancient lithospheric mantle. However, the mineral modal abundance
127 and chemical composition are somewhat different from those of Fushan and Hebi. The second
128 group of xenoliths are relatively high in olivine modal abundance and Mg-number and fall into
129 the Proterozoic field (Figure 3b). Thus, we name them "High-Mg Peridotites". The third group
130 samples belong to "Low-Mg Peridotites" due to their lower modal abundance and Mg-number of
131 olivine relative to the High-Mg ones. They follow the oceanic trend proposed by Boyd (1989)
132 and dominantly fall into the Phanerozoic field (Figure 3c). As for the fourth group, the Mg-

133 number of olivine is lower than 88, with the lowest value being as low as 80 (Figure 3d), which
 134 differs sharply from that of the sub-continental lithospheric mantle (Griffin et al., 1999). Hence,
 135 we call them “Anomalous Low-Mg Peridotite”. Among these xenoliths, “Low-Mg Peridotites”
 136 and “High-Mg Peridotites” dominate our samples (~53% and ~28% respectively), while the first
 137 group and the fourth group take ~12% and 7% of the samples, respectively. We perform
 138 discriminant analysis for those without published modal abundance data to judge whether they
 139 belong to the “High-Mg” or “Low-Mg”. In our case, the Mg-number of olivine equal to 90.5 as
 140 the group discrimination criteria is feasible. The peridotites whose olivine have Mg-number
 141 higher than 90.5 belong to “High-Mg Peridotites”. In contrast, those with olivine Mg-number
 142 between 88~90.5 belong to “Low-Mg Peridotites”.



143
 144 **Figure 2.** Petrological classification for peridotite xenoliths from the North China Craton (The
 145 detailed data are listed in **Table S1**). The brown and yellow triangle, circle, square, and diamond
 146 symbols represent the relics and those from the western NCC (WNCC), high-Mg, low-Mg, and
 147 anomalously low-Mg samples, respectively. The scheme for grouping is based on the Mg-
 148 number and modal abundance of olivine in each sample. Samples having olivine less than 50%
 149 are excluded.



150

151 **Figure 3.** Olivine Mg-number vs. modal abundance for peridotite xenoliths from the North
 152 China Craton (The detailed data are listed in **Table S1**). The oceanic trend is after Boyd (1989).
 153 The Archean, Proterozoic, and Phanerozoic fields are from Griffin et al. (1999). Symbols are the
 154 same as in Figure 2.

155 **4 Methods and Results**

156 Since all samples compiled are spinel-facies peridotites, there are no suitable geobarometers that
 157 can be used to yield reasonable pressure estimation to date. Therefore, we assume an equilibrium
 158 pressure of 1.5 GPa for subsequent calculations of temperature and oxygen fugacity.

159 **4.1 Equilibrium Temperature**

160 Many geothermometers have been calibrated to date, but not all are applicable in our study,
 161 primarily because lacking raw data for the calculation of key parameters. Therefore, we choose
 162 the two-pyroxene thermometers (Brey & Kohler, 1990; Taylor, 1998) or the enstatite-in-Cpx

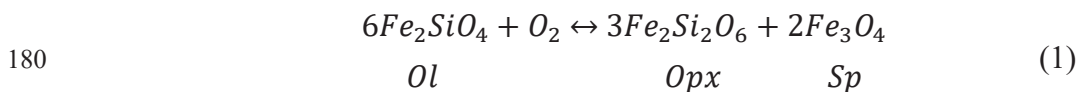
163 thermometer (Nimis & Taylor, 2000) to estimate the equilibrium temperatures of these xenoliths.
 164 For samples that are Cpx-poor or devoid of chemical compositions of Cpx, their equilibrium
 165 temperatures are calculated based on the Ol-Sp thermometer (Coogan et al., 2014).

166 As all above mentioned pyroxene-related thermometers are developed based on the similar
 167 enstatite-exchange between Opx and Cpx (Nimis & Gruetter, 2010), they yield nearly consistent
 168 outcomes within errors (Table S2). By contrast, the Ol-Sp thermometer usually gives slightly
 169 higher temperatures (Table S2).

170 The statistical results show that no matter where the peridotites are from or which group the
 171 xenoliths belong to, they all have similar temperatures (Table 1). Compared with those from the
 172 other tectonic units of the NCC, peridotites from the Trans-North China Orogen (TNCO) appear
 173 more homogeneous in temperature. Furthermore, if we project the average temperature to the
 174 geotherm of North China Craton in Mesozoic ($> 80\text{mW/m}^2$), an estimation of ~ 1.5 GPa can be
 175 inferred, confirming the reasonability of our assumption of an equilibrium pressure of 1.5 GPa
 176 for these xenoliths.

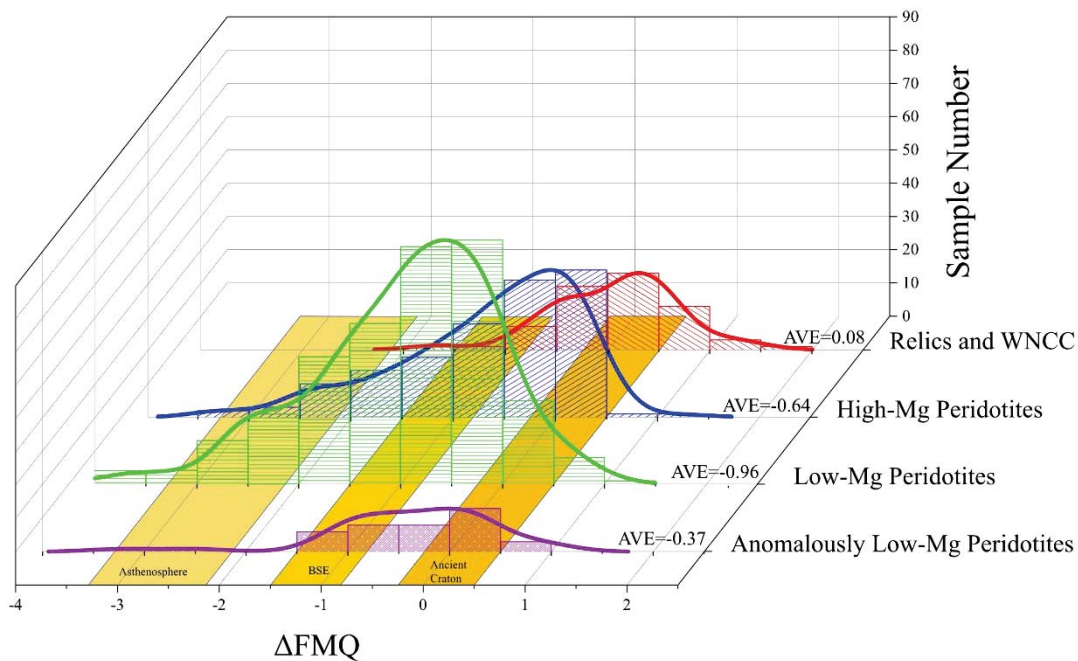
177 4.2 Oxygen Fugacity

178 Oxygen fugacity of spinel-facies peridotites is recorded by the thermodynamic equilibrium of
 179 Olivine-Orthopyroxene-Spinel assemblages (O'Neill & Wall, 1987):



181 Previous experiments have proposed two types of oxybarometers, one of which relies on the
 182 activity of Fe_3O_4 (e.g., Davis et al., 2017; Mattioli & Wood, 1988) and another requires
 183 $\text{Fe}^{3+}/\sum\text{Fe}$ by calculation assuming perfect stoichiometry (Ballhaus et al., 1991). Compared with
 184 the former equation, the advantage of the latter is that it directly links f_{O_2} to mineral
 185 compositions analyzed by EPMA, especially when Mössbauer spectroscopy is unavailable, and
 186 thus avoids correction of spinel and errors introduced during the calculating activity of magnetite
 187 end-member. Therefore, we choose the equation proposed by Ballhaus et al. (1991) to estimate
 188 the f_{O_2} .

189 The calculated oxygen fugacities of the peridotite xenoliths are shown in Figure 4 and Table 2
 190 and S2. The Ni precipitation curve reaches nearly FMQ-4 under 1.5 GPa (Frost & McCammon,
 191 2008; O'Neill & Wall, 1987), implying the appearance of Ni-bearing peridotite. Nevertheless, no
 192 Ni-bearing peridotites are reported on the NCC yet. Therefore, samples with f_{O_2} lower than
 193 FMQ-4 are excluded for further discussion. The results show that for peridotites falling into
 194 SCLM fields, f_{O_2} decreases along with lowering Mg-number (Figure 4). However, the
 195 “Anomously Low-Mg Peridotites” have relatively higher f_{O_2} , which is between the “High-Mg
 196 Peridotites” and peridotites being regarded as Archean relics and from the Western Block
 197 (Figure 4).



198
 199 **Figure 4.** The oxygen fugacity of peridotites from the North China Craton. The grouping scheme
 200 follows that in Figure 3. The data of each group shows in the form of the histogram and
 201 corresponding kernel density estimation (**the detailed data are listed in Table S2**). The oxygen
 202 fugacity of the ancient craton is extrapolated from other stable cratons (Slave Craton: Creighton
 203 et al., 2010, McCammon and Kopylova, 2004; Siberia Craton: Goncharov et al., 2012, Yaxley et
 204 al., 2012; Kaapvaal Craton: Lazarov et al., 2009, Woodland and Koch, 2003) to 1~2 GPa, under
 205 which only spinel-facies peridotites are stable. The oxygen fugacity between 1~2 GPa of the
 206 Bulk Silicate Earth (BSE) mantle is calculated via methods proposed by Stagno et al. (2013). As
 207 the Fe_2O_3 content of the asthenosphere ranges between 0.3 and 0.5 wt% (Cottrell & Kelley, 2011;

208 Sorbadere et al., 2018) and the primary melts record the same f_{O_2} to the equilibrated residues
209 (Birner et al., 2018; Davis & Cottrell, 2018), we estimate the oxygen fugacity of hypothetical
210 melts identical to the composition of the asthenosphere under 1~2 GPa and 950 °C. The average
211 oxygen fugacity of the normal mantle decreases with decreasing Mg-number of olivine.
212 However, the anomalously low-Mg peridotites are slightly more oxidized than the high-Mg and
213 low-Mg ones.

214

215 **Table 1.** Temperature estimations for peridotites from the North China Craton (the detailed data are listed in **Table S2**)

Group	Archean relics (n=47)	WNCC (n=21)	High-Mg			Low-Mg			Anomalously Low-Mg		
			TNCO (n=82)	ENCC (n=80)	Total (n=162)	TNCO (n=101)	ENCC (n=205)	Total (n=306)	TNCO (n=10)	ENCC (n=30)	Total (n=40)
Temperature (°C)	951.68	882.43	973.93	923.93	949.24	952.73	939.05	943.56	1031.69	948.36	969.19
S.D.	150.52	109.00	86.62	132.25	114.28	84.74	127.66	115.45	74.44	108.37	107.22

216

217 **Table 2.** Oxygen fugacity estimations for peridotites from the North China Craton (the detailed data are listed in **Table S2**)

Group	Archean relics (n=47)	WNCC (n=21)	High-Mg			Low-Mg			Anomalously Low-Mg		
			TNCO (n=82)	ENCC (n=80)	Total (n=162)	TNCO (n=101)	ENCC (n=205)	Total (n=306)	TNCO (n=10)	ENCC (n=30)	Total (n=40)
Δ FMQ	0.13	-0.07	-0.61	-0.67	-0.64	-1.01	-0.93	-0.96	-0.17	-0.43	-0.37
S.D.	0.59	0.64	0.83	0.91	0.87	0.93	0.89	0.90	0.87	0.77	0.80

218 **5 Discussion**

219 5.1 Oxygen fugacity of cratonic mantle

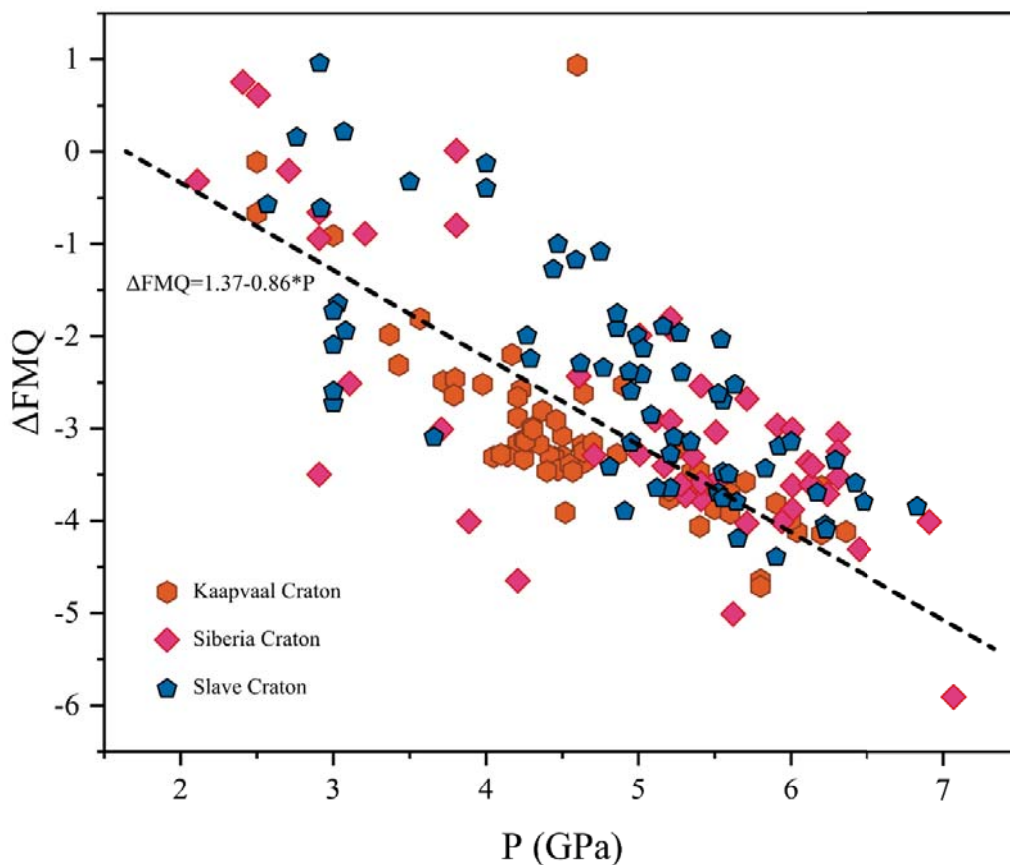
220 Before discussing how f_{O_2} of lithospheric mantle evolved during craton destruction,
 221 it is crucial to test if the peridotites of Archean relics and those from the Western
 222 Block can be treated as starting points, namely, whether their f_{O_2} resemble that of
 223 typical stable cratonic mantle lithosphere. As previous studies mainly focused on
 224 kimberlite-borne garnet-facies peridotites rather than spinel-facies ones (e.g., Lazarov
 225 et al., 2009; Woodland & Koch, 2003; Yaxley et al., 2012), to extrapolate P- $\log f_{O_2}$
 226 curves to 1~2 GPa, under which spinel-facies peridotites are stable (e.g., Till et al.,
 227 2012; Zibera et al., 2013) is a prerequisite. In theory, when coexisting spinel and
 228 garnet reach thermodynamic equilibrium, they record consistent oxygen fugacity
 229 (Miller et al., 2016). Besides, studies of Siberia Craton also support that pressure and
 230 f_{O_2} of spinel-facies and garnet-facies peridotites fit well in the same curve
 231 (Goncharov et al., 2012). McCammon and Kopylova (2004) found more reduced
 232 spinel peridotites that deviate from the P- $\log f_{O_2}$ curve in Slave Craton.
 233 Notwithstanding, this is usually interpreted to be the result of a high degree of
 234 depletion. Therefore, the extrapolation of f_{O_2} of mantle lithosphere from garnet to
 235 spinel facies is reasonable and appropriate.

236 Extrapolation of P- $\log f_{O_2}$ that combined data from Slave Craton, Siberia Craton, and
 237 Kaapvaal Craton follows the equation (Figure 5):

$$238 \quad \Delta FMQ = 1.37 - 0.86 * P \quad (2)$$

239 The gradient of the P- $\log f_{O_2}$ is similar to those reported in previous studies (Slave
 240 Craton: -0.59 log/GPa, McCammon and Kopylova, 2004; Siberia Craton: -0.83
 241 log/GPa, Goncharov et al., 2012; -1.0 log/GPa, Yaxley et al., 2012; Kaapvaal Craton:
 242 -1.0 log/GPa, Lazarov et al., 2009; and -0.86 log/GPa, Woodland and Koch, 2003).
 243 Under 1~2 GPa, the extrapolation of stable cratons' P- $\log f_{O_2}$ curve is nearly
 244 consistent with the oxygen fugacity of the first group samples, which represent relics

245 of the Archean lithospheric mantle (Figure 4). Thus, we propose that peridotites of the
 246 first group reflect the redox state of the mantle lithosphere before the destruction of
 247 the NCC. Furthermore, similar to typical stable craton around the world, peridotites
 248 from the first group have higher f_{O_2} , which could be the outcome of oxidized,
 249 sometimes multi-stage metasomatism, as evidenced by trace elements and in-situ Sr
 250 isotope of clinopyroxene (Creighton et al., 2010; Creighton et al., 2009; Dai et al.,
 251 2019; Wu et al., 2017; Xu et al., 2010; Zheng et al., 2001).



252
 253 **Figure 5.** Correlation between the oxygen fugacity and equilibrium pressure of
 254 peridotites from Kaapvaal Craton, Siberia Craton, and Slave Craton. The dashed line
 255 fitting these data serves for the oxygen fugacity extrapolation from garnet facies to
 256 spinel facies mantle. Data source: Kaapvaal Craton: Lazarov et al. (2009), Woodland
 257 and Koch (2003); Siberia Craton: Goncharov et al. (2012), Yaxley et al. (2012); Slave
 258 Craton: Creighton et al. (2010), McCammon and Kopylova (2004) (the detailed data
 259 are listed in **Table S3**).

260 5.2 Variation of oxygen fugacity during craton destruction

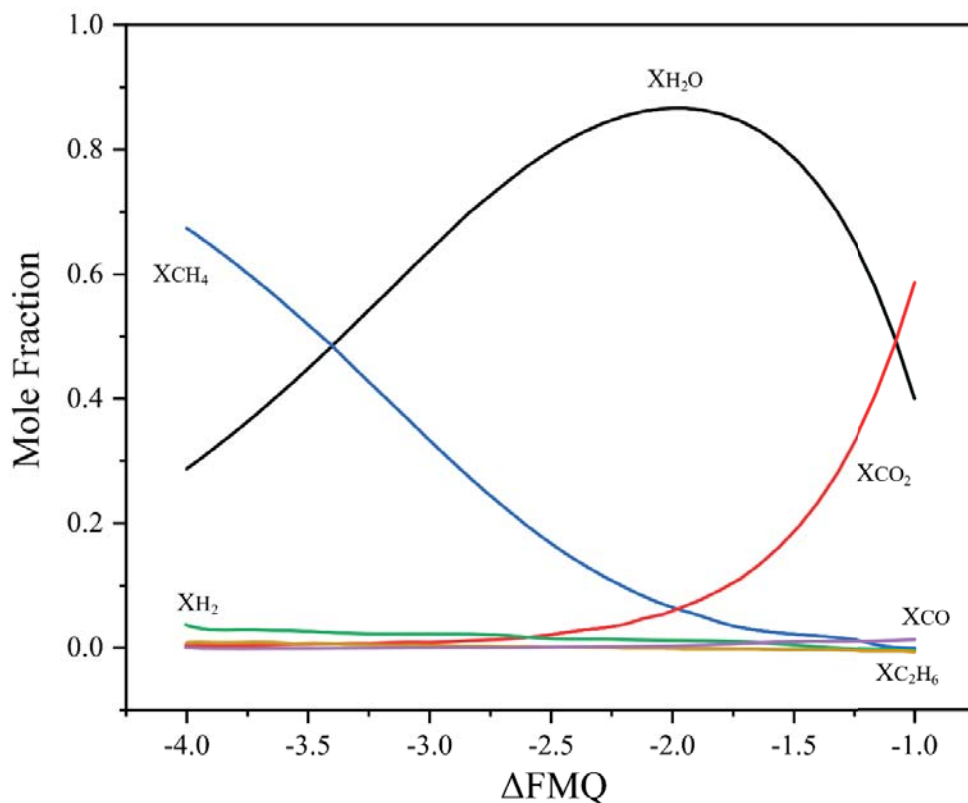
261 Craton destruction resulted from the removal or replacement of the ancient refractory
262 lithospheric keels by fertile materials (Tang et al., 2008; Xiao et al., 2010; Ying et al.,
263 2006), which is also clearly demonstrated by our observation as more than 50% of
264 samples fall into Phanerozoic fields (Figure 3). Along with craton destruction, the
265 oxygen fugacity of peridotites tends to be more reduced (Figure 4). Potential
266 mechanisms leading to the reduction of lithospheric mantle include: 1) a higher
267 degree of melt extraction (Gaillard et al., 2015), 2) metasomatism by reduced fluids
268 (Griffin et al., 2018), and 3) metasomatism by reduced melts (Creighton et al., 2010;
269 Goncharov et al., 2012).

270 In theory, the higher degree of melt extraction the mantle peridotites suffer, the lower
271 f_{O_2} the peridotite residues will record (Gaillard et al., 2015). However, the studied
272 samples with a lower degree of melt extraction, as reflected by low Mg-numbers,
273 commonly have lower oxygen fugacity (Figure 4), indicating that partial melting
274 cannot account for the reduction during craton destruction.

275 When reduced fluids (mainly CH_4+H_2O) interact with the ambient mantle, methane
276 can be oxidized to diamond (e.g., Smit et al., 2016; Thomassot et al., 2007), and the
277 lithospheric mantle will get reduced correspondingly (Griffin et al., 2018). However,
278 three lines of evidence argue against that CH_4+H_2O fluids reduced the mantle
279 lithosphere underneath the NCC. First, under the circumstance of ~ 950 °C and 1.5
280 GPa, only when f_{O_2} is lower than FMQ-3.25, the dominant species in the fluids is
281 CH_4 (Figure 6). By contrast, the f_{O_2} of most peridotites from the NCC are above
282 FMQ-2 with only minor equilibrating with CH_4 -dominated fluids (Figure 4).
283 Furthermore, if fluids and peridotites had reached an equilibrium, what can be
284 predicted is that the proportion of water caused by the oxidation of methane will
285 increase with increasing f_{O_2} , which will likely lead to an increase of water content in
286 peridotite. However, no such correlation exists in our dataset (Figure 7). Moreover,
287 the interaction of the mantle peridotites with reduced fluids would produce materials

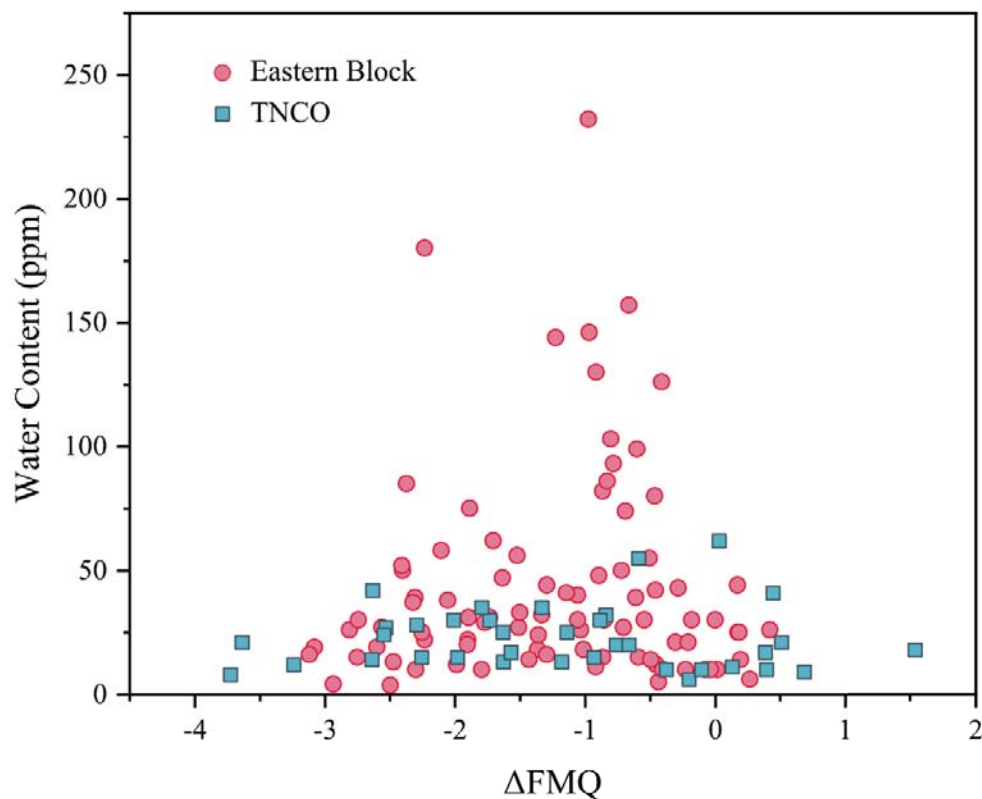
288 that reflect reduced conditions, such as diamond, SiC, and metal-alloy (Griffin et al.,
 289 2018). However, no such materials have been reported yet in peridotites entrained by
 290 Mesozoic and Cenozoic mafic rocks. Therefore, we argue that reduced fluids are
 291 highly unlikely to be the primary driving force reducing the mantle.

292



293

294 **Figure 6.** Variation of fluids species vs. oxygen fugacity under 950 °C and 1.5 GPa.
 295 The composition of fluids is calculated via GFluid (Zhang & Duan, 2009, 2010; The
 296 detailed data are listed in **Table S4**). The proportion of CH₄ increases with decreasing
 297 f_{O_2} , while CO₂ decreases with decreasing f_{O_2} . With lowering f_{O_2} , the proportion of
 298 H₂O rises and reaches the peak at $\Delta FMQ = -2$ at first and then declines. When f_{O_2}
 299 reaches $\Delta FMQ = -3.46$, the fractions of CH₄ and H₂O are identical. Other minor
 300 species (H₂, CO, and C₂H₆) show negligible variation.



301

302 **Figure 7.** Whole-rock water content vs. the oxygen fugacity of peridotite from the
 303 North China Craton. Both peridotites from the Trans-North China Orogen (TNCO)
 304 and the Eastern Block (EB) show no correlation between water content and f_{O_2} . Data
 305 source: Hao et al. (2016), Li et al. (2015), Wang et al. (2014), Xia et al. (2010), Xia et
 306 al. (2013), Yang et al. (2008). The detailed data are listed in **Table S5**.

307

308 5.3 Origin of the Anomalously Low-Mg Peridotite

309 Some samples from Yangyuan, Beiyan, Fuxin, Daxizhuang, and Longgang have very
 310 low Mg-number (generally lower than 88), inconsistent with a typical craton mantle.
 311 They are higher in f_{O_2} than all other peridotites but those of the first group (Figure 4).
 312 Therefore, an alternative process rather than metasomatism by asthenospheric
 313 materials is required to account for this anomaly.

314 Wehrlite and Cpx-rich lherzolite are preponderant in the Anomalously Low-Mg
 315 Peridotite group (Figure 2). Two modes of origin have been proposed for wehrlite,

316 including mafic-ultramafic cumulate (e.g., Mattielli et al., 1996) and product of
317 metasomatism (e.g., Gervasoni et al., 2017; Ionov et al., 2005). The wehrlite studied
318 here cannot be mafic-ultramafic cumulate because they have no cumulate texture.
319 Experiments have demonstrated that Opx-poor lherzolite and wehrlite could result
320 from the interaction between rock and silica-undersaturated basaltic melts or silicate-
321 carbonate melts. The peridotite-melt reaction could dissolve orthopyroxene while
322 generating olivine and clinopyroxene (Gervasoni et al., 2017; Kelemen et al., 1990).
323 This interpretation is reasonable because silica-undersaturated alkali basalts, which
324 are also oxidized, outcrop extensively on the NCC after ~100 Ma (Hong et al., 2020;
325 Li et al., 2017). More convincingly, Zhang et al. (2007) reported a hand-specimen
326 scale phenomenon that a wehrlite rim formed between a lherzolite and its host alkali
327 basalt. Therefore, the metasomatism of silica-undersaturated melts could lower the
328 Mg-number but raise the oxygen fugacity of the peridotites.

329 5.4 Tectonics implication

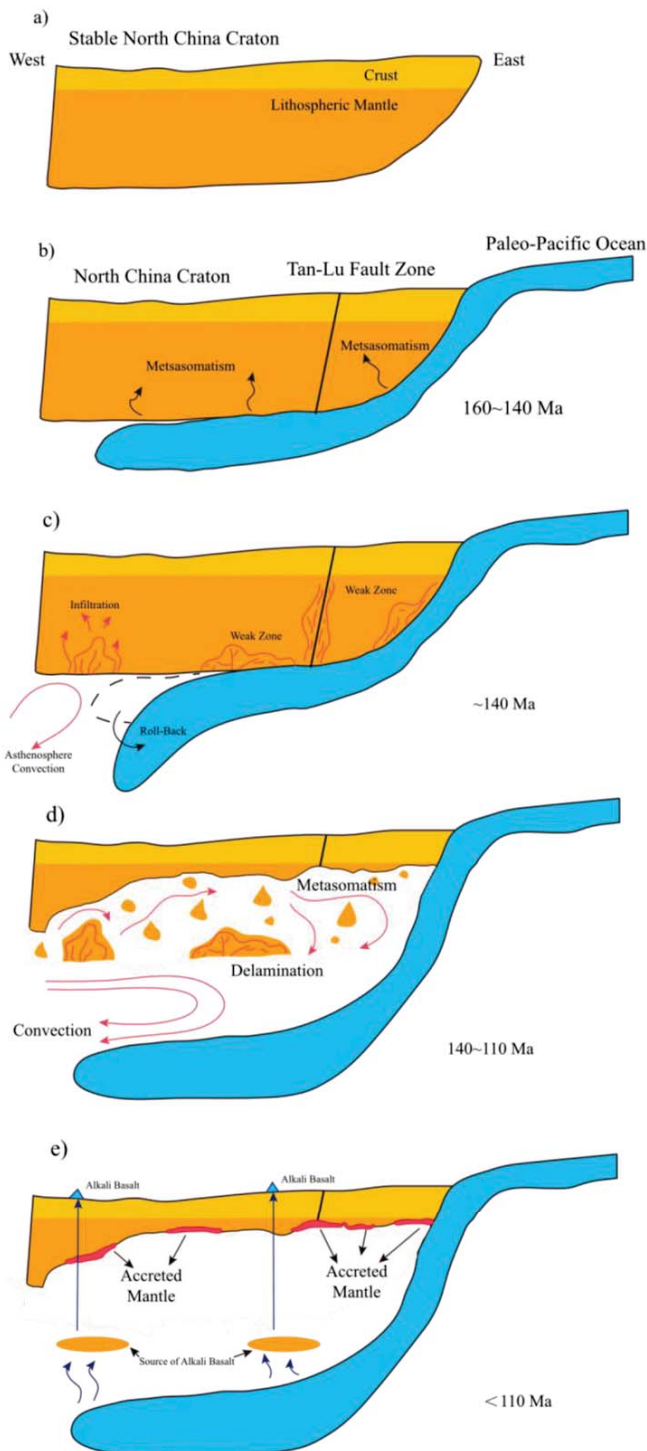
330 Peridotites have weak buffer capacity, implying their oxygen fugacity is easily reset
331 and thus only record the influence of the last metasomatism (Luth & Stachel, 2014).
332 From the view of f_{O_2} , different groups of spinel-facies peridotites from the NCC
333 jointly record multi-stage metasomatism during its evolution.

334 The first stage of evolution (Figure 8a), corresponding to the time period since the
335 final cratonization of the NCC and before the craton destruction, is recorded by the
336 first group of peridotites. Their higher Mg-number of olivine and f_{O_2} are similar to
337 those of typical stable craton (Goncharov et al., 2012), implying a high degree of melt
338 extraction and subsequent oxidized metasomatism by fluids or melts that might be
339 released during the amalgamation of the Eastern and Western Block at ca. 1.85 Ga.

340 The second stage of evolution is craton destruction (Figure 8b~e). The relics, High-
341 Mg, and Low-Mg peridotites, primarily record the interaction between the
342 asthenosphere and shallow craton lithospheric mantle, with minor direct accretion of

343 the asthenosphere. Multiple subductions, especially the Paleo-Pacific subduction and
344 subsequent slab roll-back, eroded the above lithosphere, facilitating upwelling melts'
345 infiltration and creating chemically weak zones (Foley, 2008; Wu et al., 2019). In
346 addition, the Tan-Lu fault zone, a lithosphere deep fault, also facilitates the
347 development of a physically weak zone (Xiao et al., 2010). Therefore, along with the
348 slab roll-back, the asthenosphere laterally convected to the base of the lithosphere and
349 then infiltrated and interacted with the shallow lithospheric mantle (Zheng et al.,
350 2018), resulting in the observed trend that f_{O_2} decreases with decreasing Mg-number
351 of olivine. The ancient lithospheric mantle loses its stability after being eroded or
352 even dismembered by the asthenosphere, which led to the destruction of the NCC.

353 The third stage of evolution is not a ubiquitous phenomenon and probably a locally
354 occurred process (Figure 8e). The lowering of Mg-number of olivine with increasing
355 f_{O_2} is likely attributed to the metasomatism by silica-undersaturated basaltic melts.
356 Silica-undersaturated basaltic melts that host and interact with xenoliths could
357 originate from the deep upper mantle metasomatized by melts from the stagnant
358 Pacific slab (Xu et al., 2018). The asthenosphere was involved in the metasomatism of
359 both the second and the third stages. However, the source depth of the metasomatic
360 agents ultimately determined the different outcomes. The shallow asthenosphere
361 could not have been oxidized by melts derived from the stagnant slabs, whereas the
362 deep part has. This phenomenon justifies the mantle lithosphere's vertical
363 heterogeneity (Xu et al., 2018). Moreover, the f_{O_2} profile of a reduced shallow and an
364 oxidized deep upper mantle of the NCC is in sharp contrast to typical stable cratons.



365
 366 **Figure 8.** Schematic tectonic evolution of the North China Craton (not in scale). (a)
 367 Fluids and melts derived from adjacent plates oxidized the NCC lithospheric mantle
 368 before craton destruction. (b) Fluids released by flat subduction of the Paleo-Pacific
 369 metasomatized and weakened the lithospheric mantle. (c) The subducted plate rolled

370 back, inducing mantle convection, and weak zones facilitated the infiltration of the
371 asthenospheric melts. (d) Intensive asthenosphere convection dismembered the
372 lithospheric mantle with erosion and local delamination. (e) Metasomatism of
373 asthenosphere-derived melt lowered the oxygen fugacity of the mantle lithosphere,
374 associated with minor accretion. During the Cenozoic, silica-unsaturated melts from
375 the mantle metasomatized by stagnant slab interacted with xenoliths, forming the
376 Cpx-rich lherzolites and wehrlites.

377 **6 Conclusions**

378 1. Peridotite xenoliths captured by Meso-Cenozoic basalts on the NCC record the
379 variation of oxygen fugacities in the mantle lithosphere beneath the destroyed craton.

380 2. Peridotite xenoliths from the Western Block of the NCC are relics of the Archean
381 mantle and representative of the mantle lithosphere before the craton destruction.
382 Their high f_{O_2} could result from the long-term and complicated metasomatism since
383 its cratonization and before the craton destruction.

384 3. A trend displayed by the majority of peridotite xenoliths of lowering f_{O_2} with
385 decreasing Mg-number of olivine might have resulted from extensive metasomatism
386 by melts derived from shallow asthenosphere, rather than melt extraction or
387 metasomatism by reduced fluids.

388 4. The Anomalously Low-Mg Peridotites exhibit higher f_{O_2} relative to those of the
389 Low-Mg Peridotites, suggesting that the former are probably the products of
390 metasomatism by silica-undersaturated basaltic melts derived from deep
391 asthenosphere, impinged by melts from the stagnant Pacific slab.

392 **Acknowledgments**

393 This work was financially supported by the National Natural Science Foundation of
394 China (Grant Nos. 41688103, 41725014). The authors declare that they have no
395 competing interests. All data supporting the conclusions of this paper can be found in

396 the cited references, tables, and supporting information. These data are also accessible
397 in Mendeley data [https://data.mendeley.com/datasets/k5nvgspkmf/draft?a=3863ec55-](https://data.mendeley.com/datasets/k5nvgspkmf/draft?a=3863ec55-0280-49f0-9f39-8b5d2c2e7fd9)
398 [0280-49f0-9f39-8b5d2c2e7fd9](https://data.mendeley.com/datasets/k5nvgspkmf/draft?a=3863ec55-0280-49f0-9f39-8b5d2c2e7fd9). Any real or perceived financial conflicts of interests
399 for any author

400

401 **References**

402 Ballhaus, C., Berry, R. F., & Green, D. H. (1991). High-pressure experimental
403 calibration of the olivine-ortho-pyroxene-spinel oxygen geobarometer - implications
404 for the oxidation-state of the upper mantle. *Contributions to Mineralogy and*
405 *Petrology*, *107*(1), 27-40. doi:10.1007/bf00311183

406 Birner, S. K., Cottrell, E., Warren, J. M., Kelley, K. A., & Davis, F. A. (2018).
407 Peridotites and basalts reveal broad congruence between two independent records of
408 mantle f(O₂) despite local redox heterogeneity. *Earth and Planetary Science Letters*,
409 *494*, 172-189. doi:10.1016/j.epsl.2018.04.035

410 Boyd, F. R. (1989). Compositional distinction between oceanic and cratonic
411 lithosphere. *Earth and Planetary Science Letters*, *96*(1-2), 15-26. doi:10.1016/0012-
412 821x(89)90120-9

413 Brey, G. P., & Kohler, T. (1990). Geothermobarometry in 4-phase lherzolites .2. new
414 thermobarometers, and practical assessment of existing thermobarometers. *Journal of*
415 *Petrology*, *31*(6), 1353-1378. doi:10.1093/petrology/31.6.1353

416 Canil, D., & O'Neill, H. S. C. (1996). Distribution of ferric iron in some upper-mantle
417 assemblages. *Journal of Petrology*, *37*(3), 609-635. doi:10.1093/petrology/37.3.609

418 Chen, L., Cheng, C., & Wei, Z. (2009). Seismic evidence for significant lateral
419 variations in lithospheric thickness beneath the central and western North China
420 Craton. *Earth and Planetary Science Letters*, *286*(1-2), 171-183.
421 doi:10.1016/j.epsl.2009.06.022

422 Coogan, L. A., Saunders, A. D., & Wilson, R. N. (2014). Aluminum-in-olivine

- 423 thermometry of primitive basalts: Evidence of an anomalously hot mantle source for
424 large igneous provinces. *Chemical Geology*, 368, 1-10.
425 doi:10.1016/j.chemgeo.2014.01.004
- 426 Cottrell, E., & Kelley, K. A. (2011). The oxidation state of Fe in MORB glasses and
427 the oxygen fugacity of the upper mantle. *Earth and Planetary Science Letters*, 305(3-
428 4), 270-282. doi:10.1016/j.epsl.2011.03.014
- 429 Creighton, S., Stachel, T., Eichenberg, D., & Luth, R. W. (2010). Oxidation state of
430 the lithospheric mantle beneath Diavik diamond mine, central Slave craton, NWT,
431 Canada. *Contributions to Mineralogy and Petrology*, 159(5), 645-657.
432 doi:10.1007/s00410-009-0446-x
- 433 Creighton, S., Stachel, T., Matveev, S., Hofer, H., McCammon, C., & Luth, R. W.
434 (2009). Oxidation of the Kaapvaal lithospheric mantle driven by metasomatism.
435 *Contributions to Mineralogy and Petrology*, 157(4), 491-504. doi:10.1007/s00410-
436 008-0348-3
- 437 Dai, H.-K., Zheng, J.-P., Xiong, Q., Su, Y.-P., Pan, S.-K., Ping, X.-Q., & Zhou, X.
438 (2019). Fertile lithospheric mantle underlying ancient continental crust beneath the
439 northwestern North China craton: Significant effect from the southward subduction of
440 the Paleo-Asian Ocean. *Geological Society of America Bulletin*, 131(1-2), 3-20.
441 doi:10.1130/b31871.1
- 442 Davis, F. A., & Cottrell, E. (2018). Experimental investigation of basalt and peridotite
443 oxybarometers: Implications for spinel thermodynamic models and Fe³⁺ compatibility
444 during generation of upper mantle melts. *American Mineralogist*, 103(7), 1056-1067.
445 doi:10.2138/am-2018-6280
- 446 Davis, F. A., Cottrell, E., Birner, S. K., Warren, J. M., & Lopez, O. G. (2017).
447 Revisiting the electron microprobe method of spinel-olivine-orthopyroxene
448 oxybarometry applied to spinel peridotites. *American Mineralogist*, 102(1-2), 421-
449 435. doi:10.2138/am-2017-5823
- 450 Foley, S. F. (2008). Rejuvenation and erosion of the cratonic lithosphere. *Nature*

- 451 *Geoscience*, 1(8), 503-510. doi:10.1038/ngeo261
- 452 Foley, S. F. (2011). A Reappraisal of Redox Melting in the Earth's Mantle as a
453 Function of Tectonic Setting and Time. *Journal of Petrology*, 52(7-8), 1363-1391.
454 doi:10.1093/petrology/egq061
- 455 Frost, D. J., & McCammon, C. A. (2008). The redox state of Earth's mantle. *Annual*
456 *Review of Earth and Planetary Sciences*, 36, 389-420.
457 doi:10.1146/annurev.earth.36.031207.124322
- 458 Gaillard, F., Scaillet, B., Pichavant, M., & Iacono-Marziano, G. (2015). The redox
459 geodynamics linking basalts and their mantle sources through space and time.
460 *Chemical Geology*, 418, 217-233. doi:10.1016/j.chemgeo.2015.07.030
- 461 Gervasoni, F., Klemme, S., Rohrbach, A., Gruetzner, T., & Berndt, J. (2017).
462 Experimental constraints on mantle metasomatism caused by silicate and carbonate
463 melts. *Lithos*, 282, 173-186. doi:10.1016/j.lithos.2017.03.004
- 464 Ghiorso, M. S., Hirschmann, M. M., Reiners, P. W., & Kress, V. C. (2002). The
465 pMELTS: A revision of MELTS for improved calculation of phase relations and major
466 element partitioning related to partial melting of the mantle to 3 GPa. *Geochemistry*
467 *Geophysics Geosystems*, 3. doi:10.1029/2001gc000217
- 468 Goncharov, A. G., Ionov, D. A., Doucet, L. S., & Pokhilenko, L. N. (2012). Thermal
469 state, oxygen fugacity and C-O-H fluid speciation in cratonic lithospheric mantle:
470 New data on peridotite xenoliths from the Udachnaya kimberlite, Siberia. *Earth and*
471 *Planetary Science Letters*, 357, 99-110. doi:10.1016/j.epsl.2012.09.016
- 472 Griffin, W. L., Huang, J.-X., Thomassot, E., Gain, S. E. M., Toledo, V., & O'Reilly, S.
473 Y. (2018). Super-reducing conditions in ancient and modern volcanic systems: sources
474 and behaviour of carbon-rich fluids in the lithospheric mantle. *Mineralogy and*
475 *Petrology*, 112, 101-114. doi:10.1007/s00710-018-0575-x
- 476 Griffin, W.L., O'Reilly, S.Y., Ryan, C.G., 1999. The composition and origin of sub-
477 continental lithospheric mantle. In: Fei, Y., Mysen, B.O., Berlka, C.M. (Eds.), *Mantle*

- 478 *Petrology: Field Observations and High-Pressure Experimentation: a Tribute to*
479 *Francis R. (Joe) Boyd* (pp. 13–45). Houston, TX: The Geochemical Society Special
480 Publication.
- 481 Hao, Y.-T., Xia, Q.-K., Tian, Z.-Z., & Liu, J. (2016). Mantle metasomatism did not
482 modify the initial H₂O content in peridotite xenoliths from the Tianchang basalts of
483 eastern China. *Lithos*, *260*, 315-327. doi:10.1016/j.lithos.2016.06.003
- 484 Hao, Y., Xia, Q., Liu, S., Feng, M., & Zhang, Y. (2012). Recognizing juvenile and
485 relict lithospheric mantle beneath the North China Craton: Combined analysis of H₂O,
486 major and trace elements and Sr-Nd isotope compositions of clinopyroxenes. *Lithos*,
487 *149*, 136-145. doi:10.1016/j.lithos.2012.03.013
- 488 Hong, L., Xu, Y.-G., Zhang, L., Wang, Y., & Ma, L. (2020). Recycled carbonate-
489 induced oxidization of the convective mantle beneath Jiaodong, Eastern China.
490 *Lithos*, *366*. doi:10.1016/j.lithos.2020.105544
- 491 Ionov, D. A., Chanefo, I., & Bodinier, J. L. (2005). Origin of Fe-rich lherzolites and
492 wehrlites from Tok, SE Siberia by reactive melt percolation in refractory mantle
493 peridotites. *Contributions to Mineralogy and Petrology*, *150*(3), 335-353.
494 doi:10.1007/s00410-005-0026-7
- 495 Kelemen, P. B., Joyce, D. B., Webster, J. D., & Holloway, J. R. (1990). Reaction
496 between ultramafic rock and fractionating basaltic magma .2. Experimental
497 investigation of reaction between olivine tholeiite and harzburgite at 1150 °C-1050 °C
498 and 5 kb. *Journal of Petrology*, *31*(1), 99-134. doi:10.1093/petrology/31.1.99
- 499 Lazarov, M., Woodland, A. B., & Brey, G. P. (2009). Thermal state and redox
500 conditions of the Kaapvaal mantle: A study of xenoliths from the Finsch mine, South
501 Africa. *Lithos*, *112*, 913-923. doi:10.1016/j.lithos.2009.03.035
- 502 Li, P., Xia, Q.-K., Deloule, E., Chen, H., Gu, X.-Y., & Feng, M. (2015). Temporal
503 variation of H₂O content in the lithospheric mantle beneath the eastern North China
504 Craton: Implications for the destruction of cratons. *Gondwana Research*, *28*(1), 276-
505 287. doi:10.1016/j.gr.2014.03.012

- 506 Li, S.-G., Yang, W., Ke, S., Meng, X., Tian, H., Xu, L., . . . Yan, J. (2017). Deep
507 carbon cycles constrained by a large-scale mantle Mg isotope anomaly in eastern
508 China. *National Science Review*, 4(1), 111-120. doi:10.1093/nsr/nww070
- 509 Liu, D. Y., Nutman, A. P., Compston, W., Wu, J. S., & Shen, Q. H. (1992). Remnants
510 of greater-than-or-equal-to 3800 ma crust in the chinese part of the sino-korean
511 craton. *Geology*, 20(4), 339-342. doi:10.1130/0091-
512 7613(1992)020<0339:Romcit>2.3.Co;2
- 513 Liu, J., Rudnick, R. L., Walker, R. J., Gao, S., Wu, F.-y., Piccoli, P. M., . . . Xu, Y.-G.
514 (2011). Mapping lithospheric boundaries using Os isotopes of mantle xenoliths: An
515 example from the North China Craton. *Geochimica Et Cosmochimica Acta*, 75(13),
516 3881-3902. doi:10.1016/j.gca.2011.04.018
- 517 Luth, R. W., & Stachel, T. (2014). The buffering capacity of lithospheric mantle:
518 implications for diamond formation. *Contributions to Mineralogy and Petrology*,
519 168(5). doi:10.1007/s00410-014-1083-6
- 520 Mattielli, N., Weis, D., Gregoire, M., Mennessier, J. P., Cottin, J. Y., & Giret, A.
521 (1996). Kerguelen basic and ultrabasic xenoliths: Evidence for long-lived Kerguelen
522 hotspot activity. *Lithos*, 37(2-3), 261-280. doi:10.1016/0024-4937(95)00040-2
- 523 Mattioli, G. S., & Wood, B. J. (1988). Magnetite activities across the MgAl₂O₄-Fe₃O₄
524 spinel join, with application to thermobarometric estimates of upper mantle oxygen
525 fugacity. *Contributions to Mineralogy and Petrology*, 98(2), 148-162.
526 doi:10.1007/bf00402108
- 527 McCammon, C., & Kopylova, M. G. (2004). A redox profile of the Slave mantle and
528 oxygen fugacity control in the cratonic mantle. *Contributions to Mineralogy and*
529 *Petrology*, 148(1), 55-68. doi:10.1007/s00410-004-0583-1
- 530 Menzies, M. A., & Xu, Y. G. (1998). Geodynamics of the North China Craton. In M.
531 F. J. Flower, S. L. Chung, C. H. Lo, & T. Y. Lee (Eds.), *Mantle Dynamics and Plate*
532 *Interactions in East Asia* (Vol. 27, pp. 155-165).

- 533 Miller, W. G. R., Holland, T. J. B., & Gibson, S. A. (2016). Garnet and Spinel
534 Oxybarometers: New Internally Consistent Multi-equilibria Models with Applications
535 to the Oxidation State of the Lithospheric Mantle. *Journal of Petrology*, 57(6), 1199-
536 1222. doi:10.1093/petrology/egw037
- 537 Nimis, P., & Gruetter, H. (2010). Internally consistent geothermometers for garnet
538 peridotites and pyroxenites. *Contributions to Mineralogy and Petrology*, 159(3), 411-
539 427. doi:10.1007/s00410-009-0455-9
- 540 Nimis, P., & Taylor, W. R. (2000). Single clinopyroxene thermobarometry for garnet
541 peridotites. Part I. Calibration and testing of a Cr-in-Cpx barometer and an enstatite-
542 in-Cpx thermometer. *Contributions to Mineralogy and Petrology*, 139(5), 541-554.
543 doi:10.1007/s004100000156
- 544 Norman, M. D. (1998). Melting and metasomatism in the continental lithosphere:
545 laser ablation ICPMS analysis of minerals in spinel lherzolites from eastern Australia.
546 *Contributions to Mineralogy and Petrology*, 130(3-4), 240-255.
547 doi:10.1007/s004100050363
- 548 O'Neill, H. S., & Wall, V. J. (1987). The Olivine-Orthopyroxene-Spinel oxygen
549 geobarometer, the nickel precipitation curve, and the oxygen fugacity of the earths
550 upper mantle. *Journal of Petrology*, 28(6), 1169-1191.
551 doi:10.1093/petrology/28.6.1169
- 552 Smit, K. V., Shirey, S. B., Stern, R. A., Steele, A., & Wang, W. (2016). Diamond
553 growth from C-H-N-O recycled fluids in the lithosphere: Evidence from CH₄ micro-
554 inclusions and $\delta^{13}\text{C}$ - $\delta^{15}\text{N}$ -N content in Marange mixed-habit diamonds. *Lithos*, 265,
555 68-81. doi:10.1016/j.lithos.2016.03.015
- 556 Sorbadere, F., Laurenz, V., Frost, D. J., Wenz, M., Rosenthal, A., McCammon, C., &
557 Rivard, C. (2018). The behaviour of ferric iron during partial melting of peridotite.
558 *Geochimica Et Cosmochimica Acta*, 239, 235-254. doi:10.1016/j.gca.2018.07.019
- 559 Stagno, V., Ojwang, D. O., McCammon, C. A., & Frost, D. J. (2013). The oxidation
560 state of the mantle and the extraction of carbon from Earth's interior. *Nature*,

- 561 493(7430), 84-+. doi:10.1038/nature11679
- 562 Sun, C., & Dasgupta, R. (2020). Thermobarometry of CO₂-rich, silica-undersaturated
563 melts constrains cratonic lithosphere thinning through time in areas of kimberlitic
564 magmatism. *Earth and Planetary Science Letters*, 550.
565 doi:10.1016/j.epsl.2020.116549
- 566 Tang, Y.-J., Zhang, H.-F., Ying, J.-F., Zhang, J., & Liu, X.-M. (2008). Refertilization
567 of ancient lithospheric mantle beneath the central North China Craton: Evidence from
568 petrology and geochemistry of peridotite xenoliths. *Lithos*, 101(3-4), 435-452.
569 doi:10.1016/j.lithos.2007.09.006
- 570 Taylor, W. R. (1998). An experimental test of some geothermometer and
571 geobarometer formulations for upper mantle peridotites with application to the
572 thermobarometry of fertile Iherzolite and garnet websterite. *Neues Jahrbuch Fur*
573 *Mineralogie-Abhandlungen*, 172(2-3), 381-408. Retrieved from <Go to
574 ISI>://WOS:000073997000016
- 575 Thomassot, E., Cartigny, P., Harris, J. W., & Viljoen, K. S. (2007). Methane-related
576 diamond crystallization in the Earth's mantle: Stable isotope evidences from a single
577 diamond-bearing xenolith. *Earth and Planetary Science Letters*, 257(3-4), 362-371.
578 doi:10.1016/j.epsl.2007.02.020
- 579 Till, C. B., Grove, T. L., & Krawczynski, M. J. (2012). A melting model for variably
580 depleted and enriched Iherzolite in the plagioclase and spinel stability fields. *Journal*
581 *of Geophysical Research-Solid Earth*, 117. doi:10.1029/2011jb009044
- 582 Wang, Q., Bagdassarov, N., Xia, Q.-K., & Zhu, B. (2014). Water contents and
583 electrical conductivity of peridotite xenoliths from the North China Craton:
584 Implications for water distribution in the upper mantle. *Lithos*, 189, 105-126.
585 doi:10.1016/j.lithos.2013.08.005
- 586 Woodland, A. B., & Koch, M. (2003). Variation in oxygen fugacity with depth in the
587 upper mantle beneath the Kaapvaal craton, Southern Africa. *Earth and Planetary*
588 *Science Letters*, 214(1-2), 295-310. doi:10.1016/s0012-821x(03)00379-0

- 589 Woodland, A. B., Kornprobst, J., & Tabit, A. (2006). Ferric iron in orogenic lherzolite
590 massifs and controls of oxygen fugacity in the upper mantle. *Lithos*, 89(1-2), 222-241.
591 doi:10.1016/j.lithos.2005.12.014
- 592 Workman, R. K., & Hart, S. R. (2005). Major and trace element composition of the
593 depleted MORB mantle (DMM). *Earth and Planetary Science Letters*, 231(1-2), 53-
594 72. doi:10.1016/j.epsl.2004.12.005
- 595 Wu, D., Liu, Y., Chen, C., Xu, R., Ducea, M. N., Hu, Z., & Zong, K. (2017). In-situ
596 trace element and Sr isotopic compositions of mantle xenoliths constrain two-stage
597 metasomatism beneath the northern North China Craton. *Lithos*, 288, 338-351.
598 doi:10.1016/j.lithos.2017.07.018
- 599 Wu, F.-Y., Yang, J.-H., Xu, Y.-G., Wilde, S. A., & Walker, R. J. (2019). Destruction of
600 the North China Craton in the Mesozoic. In R. Jeanloz & K. H. Freeman (Eds.),
601 *Annual Review of Earth and Planetary Sciences, Vol 47* (Vol. 47, pp. 173-+).
- 602 Xia, Q.-K., Hao, Y.-T., Liu, S.-C., Gu, X.-Y., & Feng, M. (2013). Water contents of
603 the Cenozoic lithospheric mantle beneath the western part of the North China Craton:
604 Peridotite xenolith constraints. *Gondwana Research*, 23(1), 108-118.
605 doi:10.1016/j.gr.2012.01.010
- 606 Xia, Q.-K., Hao, Y., Li, P., Deloule, E., Coltorti, M., Dallai, L., . . . Feng, M. (2010).
607 Low water content of the Cenozoic lithospheric mantle beneath the eastern part of the
608 North China Craton. *Journal of Geophysical Research-Solid Earth*, 115.
609 doi:10.1029/2009jb006694
- 610 Xiao, Y., Zhang, H.-F., Fan, W.-M., Ying, J.-F., Zhang, J., Zhao, X.-M., & Su, B.-X.
611 (2010). Evolution of lithospheric mantle beneath the Tan-Lu fault zone, eastern North
612 China Craton: Evidence from petrology and geochemistry of peridotite xenoliths.
613 *Lithos*, 117(1-4), 229-246. doi:10.1016/j.lithos.2010.02.017
- 614 Xu, W., Yang, D., Gao, S., Pei, F., & Yu, Y. (2010). Geochemistry of peridotite
615 xenoliths in Early Cretaceous high-Mg# diorites from the Central Orogenic Block of
616 the North China Craton: The nature of Mesozoic lithospheric mantle and constraints

- 617 on lithospheric thinning. *Chemical Geology*, 270(1-4), 257-273.
618 doi:10.1016/j.chemgeo.2009.12.006
- 619 Xu, Y., Li, H., Hong, L., Ma, L., Ma, Q., & Sun, M. (2018). Generation of Cenozoic
620 intraplate basalts in the big mantle wedge under eastern Asia. *Science China-Earth*
621 *Sciences*, 61(7), 869-886. doi:10.1007/s11430-017-9192-y
- 622 Yang, X.-Z., Xia, Q.-K., Deloule, E., Dallai, L., Fan, Q.-C., & Feng, M. (2008). Water
623 in minerals of the continental lithospheric mantle and overlying lower crust: A
624 comparative study of peridotite and granulite xenoliths from the North China Craton.
625 *Chemical Geology*, 256(1-2), 33-45. doi:10.1016/j.chemgeo.2008.07.020
- 626 Yaxley, G. M., Berry, A. J., Kamenetsky, V. S., Woodland, A. B., & Golovin, A. V.
627 (2012). An oxygen fugacity profile through the Siberian Craton - Fe K-edge XANES
628 determinations of $\text{Fe}^{3+}/\Sigma\text{Fe}$ in garnets in peridotite xenoliths from the Udachnaya East
629 kimberlite. *Lithos*, 140, 142-151. doi:10.1016/j.lithos.2012.01.016
- 630 Ying, J. F., Zhang, H. F., Kita, N., Morishita, Y., & Shimoda, G. (2006). Nature and
631 evolution of late cretaceous lithospheric mantle beneath the eastern North China
632 Craton: Constraints from petrology and geochemistry of peridotitic xenoliths from
633 Junan, Shandong Province, China. *Earth and Planetary Science Letters*, 244(3-4),
634 622-638. doi:10.1016/j.epsl.2006.02.023
- 635 Zhang, C., & Duan, Z. (2009). A model for C-O-H fluid in the Earth's mantle.
636 *Geochimica Et Cosmochimica Acta*, 73(7), 2089-2102. doi:10.1016/j.gca.2009.01.021
- 637 Zhang, C., & Duan, Z. (2010). GFluid: An Excel spreadsheet for investigating C-O-H
638 fluid composition under high temperatures and pressures. *Computers & Geosciences*,
639 36(4), 569-572. doi:10.1016/j.cageo.2009.05.008
- 640 Zhang, H.-F., Nakamura, E., Sun, M., Kobayashi, K., Zhang, J., Ying, J.-F., . . . Niu,
641 L.-F. (2007). Transformation of subcontinental lithospheric mantle through peridotite-
642 melt reaction: Evidence from a highly fertile mantle xenolith from the north China
643 Craton. *International Geology Review*, 49(7), 658-679. doi:10.2747/0020-
644 6814.49.7.658

- 645 Zhao, G. C., Sun, M., Wilde, S. A., & Li, S. Z. (2005). Late Archean to
646 Paleoproterozoic evolution of the North China Craton: key issues revisited.
647 *Precambrian Research*, 136(2), 177-202. doi:10.1016/j.precamres.2004.10.002
- 648 Zheng, J., Griffin, W. L., O'Reilly, S. Y., Yang, J., Li, T., Zhang, M., . . . Liou, J. G.
649 (2006). Mineral chemistry of peridotites from Paleozoic, Mesozoic and Cenozoic
650 lithosphere: Constraints on mantle evolution beneath eastern China. *Journal of*
651 *Petrology*, 47(11), 2233-2256. doi:10.1093/petrology/egl042
- 652 Zheng, J. P., Griffin, W. L., Ma, Q., O'Reilly, S. Y., Xiong, Q., Tang, H. Y., . . . Su, Y.
653 P. (2012). Accretion and reworking beneath the North China Craton. *Lithos*, 149, 61-
654 78. doi:10.1016/j.lithos.2012.04.025
- 655 Zheng, J. P., O'Reilly, S. Y., Griffin, W. L., Lu, F. X., Zhang, M., & Pearson, N. J.
656 (2001). Relict refractory mantle beneath the eastern North China block: significance
657 for lithosphere evolution. *Lithos*, 57(1), 43-66. doi:10.1016/s0024-4937(00)00073-6
- 658 Zheng, Y., Xu, Z., Zhao, Z., & Dai, L. (2018). Mesozoic mafic magmatism in North
659 China: Implications for thinning and destruction of cratonic lithosphere. *Science*
660 *China-Earth Sciences*, 61(4), 353-385. doi:10.1007/s11430-017-9160-3
- 661 Ziberna, L., Klemme, S., & Nimis, P. (2013). Garnet and spinel in fertile and depleted
662 mantle: insights from thermodynamic modelling. *Contributions to Mineralogy and*
663 *Petrology*, 166(2), 411-421. doi:10.1007/s00410-013-0882-5

664 **References From the Supporting Information**

- 665 Chen, J. C., Hsu, C. N., & Ho, K. S. (2003). Geochemistry of Cenozoic volcanic rocks and
666 related ultramafic xenoliths from the Jilin and Heilongjiang provinces, northeast China. *Journal*
667 *of Asian Earth Sciences*, 21(9), 1069-1084. doi:10.1016/s1367-9120(02)00144-x
- 668 Chen, S. H., O'Reilly, S. Y., Zhou, X. H., Griffin, W. L., Zhang, G. H., Sun, M., . . . Zhang, M.
669 (2001). Thermal and petrological structure of the lithosphere beneath Hannuoba, Sino-Korean
670 Craton, China: evidence from xenoliths. *Lithos*, 56(4), 267-301. doi:10.1016/s0024-
671 4937(00)00065-7
- 672 Chu, Z.-Y., Wu, F.-Y., Walker, R. J., Rudnick, R. L., Pitcher, L., Puchtel, I. S., . . . Wilde, S. A.
673 (2009). Temporal Evolution of the Lithospheric Mantle beneath the Eastern North China Craton.
674 *Journal of Petrology*, 50(10), 1857-1898. doi:10.1093/petrology/egp055
- 675 Deng, L., Liu, Y., Zong, K., Zhu, L., Xu, R., Hu, Z., & Gao, S. (2017). Trace element and Sr
676 isotope records of multi-episode carbonatite metasomatism on the eastern margin of the North
677 China Craton. *Geochemistry Geophysics Geosystems*, 18(1), 220-237.
678 doi:10.1002/2016gc006618
- 679 Hong, L.-B., Xu, Y.-G., Ren, Z.-Y., Kuang, Y.-S., Zhang, Y.-L., Li, J., . . . Zhang, H. (2012).
680 Petrology, geochemistry and Re-Os isotopes of peridotite xenoliths from Yantai, Shandong
681 Province: Evidence for Phanerozoic lithospheric mantle beneath eastern North China Craton.
682 *Lithos*, 155, 256-271. doi:10.1016/j.lithos.2012.09.005
- 683 Hu, Y., Teng, F.-Z., Zhang, H.-F., Xiao, Y., & Su, B.-X. (2016). Metasomatism-induced mantle
684 magnesium isotopic heterogeneity: Evidence from pyroxenites. *Geochimica Et Cosmochimica*
685 *Acta*, 185, 88-111. doi:10.1016/j.gca.2015.11.001
- 686 Liu, J., Carlson, R. W., Rudnick, R. L., Walker, R. J., Gao, S., & Wu, F.-Y. (2012). Comparative
687 Sr-Nd-Hf-Os-Pb isotope systematics of xenolithic peridotites from Yangyuan, North China
688 Craton: Additional evidence for a Paleoproterozoic age. *Chemical Geology*, 332, 1-14.
689 doi:10.1016/j.chemgeo.2012.09.013
- 690 Rudnick, R. L., Shan, G., Ling, W. L., Liu, Y. S., & McDonough, W. F. (2004). Petrology and
691 geochemistry of spinel peridotite xenoliths from Hannuoba and Qixia, North China Craton.
692 *Lithos*, 77(1-4), 609-637. doi:10.1016/j.lithos.2004.03.033

- 693 Tang, Y.-J., Zhang, H.-F., Deloule, E., Su, B.-X., Ying, J.-F., Xiao, Y., & Hu, Y. (2012). Slab-
694 derived lithium isotopic signatures in mantle xenoliths from northeastern North China Craton.
695 *Lithos*, 149, 79-90. doi:10.1016/j.lithos.2011.12.001
- 696 Tang, Y.-J., Zhang, H.-F., Nakamura, E., Moriguti, T., Kobayashi, K., & Ying, J.-F. (2007).
697 Lithium isotopic systematics of peridotite xenoliths from Hannuoba, North China Craton:
698 Implications for melt-rock interaction in the considerably thinned lithospheric mantle.
699 *Geochimica Et Cosmochimica Acta*, 71(17), 4327-4341. doi:10.1016/j.gca.2007.07.006
- 700 Wang, C., Liu, Y., Foley, S. F., Zong, K., & Hu, Z. (2019). Lithospheric transformation of the
701 northern North China Craton by changing subduction style of the Paleo-Asian oceanic plate:
702 Constraints from peridotite and pyroxenite xenoliths in the Yangyuan basalts. *Lithos*, 328, 58-68.
703 doi:10.1016/j.lithos.2019.01.018
- 704 Wu, F.-Y., Walker, R. J., Yang, Y.-H., Yuan, H.-L., & Yang, J.-H. (2006). The chemical-temporal
705 evolution of lithospheric mantle underlying the North China Craton. *Geochimica Et*
706 *Cosmochimica Acta*, 70(19), 5013-5034. doi:10.1016/j.gca.2006.07.014
- 707 Xu, Q., Liu, J., He, H., & Zhang, Y. (2019). Nature and evolution of the lithospheric mantle
708 revealed by water contents and He-Ar isotopes of peridotite xenoliths from Changbaishan and
709 Longgang basalts in Northeast China. *Science Bulletin*, 64(18), 1325-1335.
710 doi:10.1016/j.scib.2019.07.006
- 711 Xu, Y. G., & Bodinier, J. L. (2004). Contrasting enrichments in high- and low-temperature
712 mantle xenoliths from Nushan, eastern China: Results of a single metasomatic event during
713 lithospheric accretion? *Journal of Petrology*, 45(2), 321-341. doi:10.1093/petrology/egg098
- 714 Yang, J.-H., Zhang, M., & Wu, F.-Y. (2018). Mesozoic decratonization of the North China Craton
715 by lithospheric delamination: Evidence from Sr-Nd-Hf-Os isotopes of mantle xenoliths of
716 Cenozoic alkaline basalts in Yangyuan, Hebei Province, China. *Journal of Asian Earth Sciences*,
717 160, 396-407. doi:10.1016/j.jseaes.2017.09.002
- 718 Zhang, J., Zhang, H., Kita, N., Shimoda, G., Morishita, Y., Ying, J., & Tang, Y. (2011). Secular
719 evolution of the lithospheric mantle beneath the eastern North China craton: evidence from
720 peridotitic xenoliths from Late Cretaceous mafic rocks in the Jiaodong region, east-central
721 China. *International Geology Review*, 53(2), 182-211. doi:10.1080/00206810903025090

- 722 Zhao, X.-M., Zhang, H.-F., Zhu, X.-K., Zhu, B., & Cao, H.-h. (2015). Effects of melt percolation
723 on iron isotopic variation in peridotites from Yangyuan, North China Craton. *Chemical Geology*,
724 *401*, 96-110. doi:10.1016/j.chemgeo.2015.02.031
- 725 Zhao, X., Wang, H., Li, Z., Liu, F., Evans, N. J., & Zhang, H. (2020). Multi-stage metasomatism
726 of lithospheric mantle by asthenosphere-derived melts: evidence from mantle xenoliths in
727 daxizhuang at the eastern North China craton. *Mineralogy and Petrology*, *114*(2), 141-159.
728 doi:10.1007/s00710-020-00697-w
- 729 Zhao, X., Zhang, H., Zhu, X., Tang, S., & Tang, Y. (2010). Iron isotope variations in spinel
730 peridotite xenoliths from North China Craton: implications for mantle metasomatism.
731 *Contributions to Mineralogy and Petrology*, *160*(1), 1-14. doi:10.1007/s00410-009-0461-y
- 732 Zheng, J., Griffin, W. L., O'Reilly, S. Y., Yang, J., Li, T., Zhang, M., . . . Liou, J. G. (2006).
733 Mineral chemistry of peridotites from Paleozoic, Mesozoic and Cenozoic lithosphere:
734 Constraints on mantle evolution beneath eastern China. *Journal of Petrology*, *47*(11), 2233-2256.
735 doi:10.1093/petrology/egl042
- 736 Zheng, J. P., Griffin, W. L., O'Reilly, S. Y., Yu, C. M., Zhang, H. F., Pearson, N., & Zhang, M.
737 (2007). Mechanism and timing of lithospheric modification and replacement beneath the eastern
738 North China Craton: Peridotitic xenoliths from the 100 Ma Fuxin basalts and a regional
739 synthesis. *Geochimica Et Cosmochimica Acta*, *71*(21), 5203-5225.
740 doi:10.1016/j.gca.2007.07.028
- 741 Zheng, J. P., O'Reilly, S. Y., Griffin, W. L., Lu, F. X., & Zhang, M. (1998). Nature and evolution
742 of Cenozoic lithospheric mantle beneath Shandong peninsula, Sino-Korean craton, eastern
743 China. *International Geology Review*, *40*(6), 471-499. doi:10.1080/00206819809465220
- 744 Zou, D., Zhang, H., Hu, Z., & Santosh, M. (2016). Complex metasomatism of lithospheric
745 mantle by asthenosphere-derived melts: Evidence from peridotite xenoliths in Weichang at the
746 northern margin of the North China Craton. *Lithos*, *264*, 210-223.
747 doi:10.1016/j.lithos.2016.08.036
- 748 Zou, D., Zhang, H., Zhang, X., Zhang, H., & Su, B. (2020). Refertilization of lithospheric mantle
749 beneath the North China Craton in Mesozoic: Evidence from in situ Sr isotopes of Fuxin
750 peridotite. *Lithos*, *364*. doi:10.1016/j.lithos.2020.10547

751

752

Oxygen fugacity evolution of the mantle lithosphere beneath the North China craton

Chen-Yang Ye^{1,2}, Ji-Feng Ying^{1,2,3*}, Yan-Jie Tang^{1,2,3}, Xin-Miao Zhao^{1,3}, Hong-Fu Zhang^{1,2,3}

1. State Key Laboratory of Lithospheric Evolution, Institute of Geology and Geophysics, Chinese Academy of Sciences, Beijing 100029, China
2. College of Earth and Planetary Sciences, University of Chinese Academy of Sciences, Beijing 100049, China
3. Innovation Academy for Earth Science, Chinese Academy of Sciences, Beijing 100029, China

Contents of this file

Text S1
Figures S1

Additional Supporting Information (Files uploaded separately)

Captions for Datasets S1
Captions for Tables S1 to S7

Introduction

This supporting information contains specific references of our research (Text S1) and histograms that show the modeled partial melting degree the Low-Mg peridotites had experienced (Figure S1). The detailed major elemental compositions for peridotite minerals (Ol, Opx, Cpx, and Sp) are listed in Dataset S1. Tables S1 to S7 compile the data for Figure 2 to 7 in the main text.

Text S1. References of peridotites referred in this study

Location (Sample Number)	Age ¹ (Ma)	Reference
Trans-North China Orogen		
Hannuoba (n=53)	27~14 Ma	Chen et al. (2001)
		Hu et al. (2016)
		Liu et al. (2011)
		Rudnick et al. (2004)
		Tang et al. (2007)
		Wang et al. (2014)
		Yang et al. (2008)
		Zhao et al. (2010)
Yangyuan (n=94)	35~30 Ma	Hao et al. (2012)
		Liu et al. (2011)
		Liu et al. (2012)
		Wang et al. (2014)
		Wang et al. (2019)
		Xia et al. (2013)
		Yang et al. (2018)
		Zhao et al. (2015)
Datong (n=5)	~1 Ma	Liu et al. (2011)
Fanshi (n=37)	~25 Ma	Liu et al. (2011)
		Tang et al. (2008)
		Xia et al. (2013)
Hebi (n=35)	~4 Ma	Liu et al. (2011)
		Wang et al. (2014)
		Xia et al. (2010)
		Zhao et al. (2010)
		Zheng et al. (2001)
Fushan (n=10)	~125 Ma	Liu et al. (2011)
		Xu et al. (2010)
Weichang (n=12)	23~5.2 Ma	Zou et al. (2016)
Northeast China		
Longgang (n=17)	0.68~0.05 Ma	Chen et al. (2003)
		Tang et al. (2012)
		Xu et al. (2019)
Kuandian (n=10)	~0.6 Ma	Wu et al. (2006)
Changbaishan (n=12)	19.9~2.6 Ma	Xu et al. (2019)
Fuxin	~100 Ma	Zheng et al. (2007)

(n=25)		Zou et al. (2020)
Shandong-Talu Fault Zone		
Penglai (n=20)	~8 Ma	Chu et al. (2009) Xia et al. (2010)
Shanwang (n=33)	~16 Ma	Chu et al. (2009) Zheng et al. (1998) Zheng et al. (2006)
Changle (n=24)	18~9 Ma	Deng et al. (2017) Xia et al. (2010)
Yantai (n=11)	~7.4 Ma	Hong et al. (2012)
Tianchang (n=15)	~9 Ma	Hao et al. (2016)
Junan (n=22)	~67 Ma	Li et al. (2015) Ying et al. (2006)
Daxizhuang (n=19)	~74 Ma	Li et al. (2015) Zhang et al. (2007) Zhao et al. (2020)
Pishikou (n=28)	~82 Ma	Li et al. (2015) Zhang et al. (2011)
Qixia (n=25)	~6 Ma	Rudnick et al. (2004) Xia et al. (2010) Zheng et al. (1998)
Nvshan (n=23)	~2 Ma	Wang et al. (2014) Xu et al. (2004) Yang et al. (2008)
Panshishan (n=10)	~9 Ma	Xia et al. (2010)
Lianshan (n=15)	~9 Ma	Xia et al. (2010)
Fangshan (n=13)	~9 Ma	Xia et al. (2010)
Beiyan (n=22)	18.8~10.8 Ma	Xiao et al. (2010)
Western North china Craton		
Langshan (n=7)	~89 Ma	Dai et al. (2019)
Jining (n=11)	~32 Ma	Liu et al. (2011)
Dongbahao (n=6)	23.54~20.24 Ma	Wu et al. (2017)

¹ The age of the host rocks

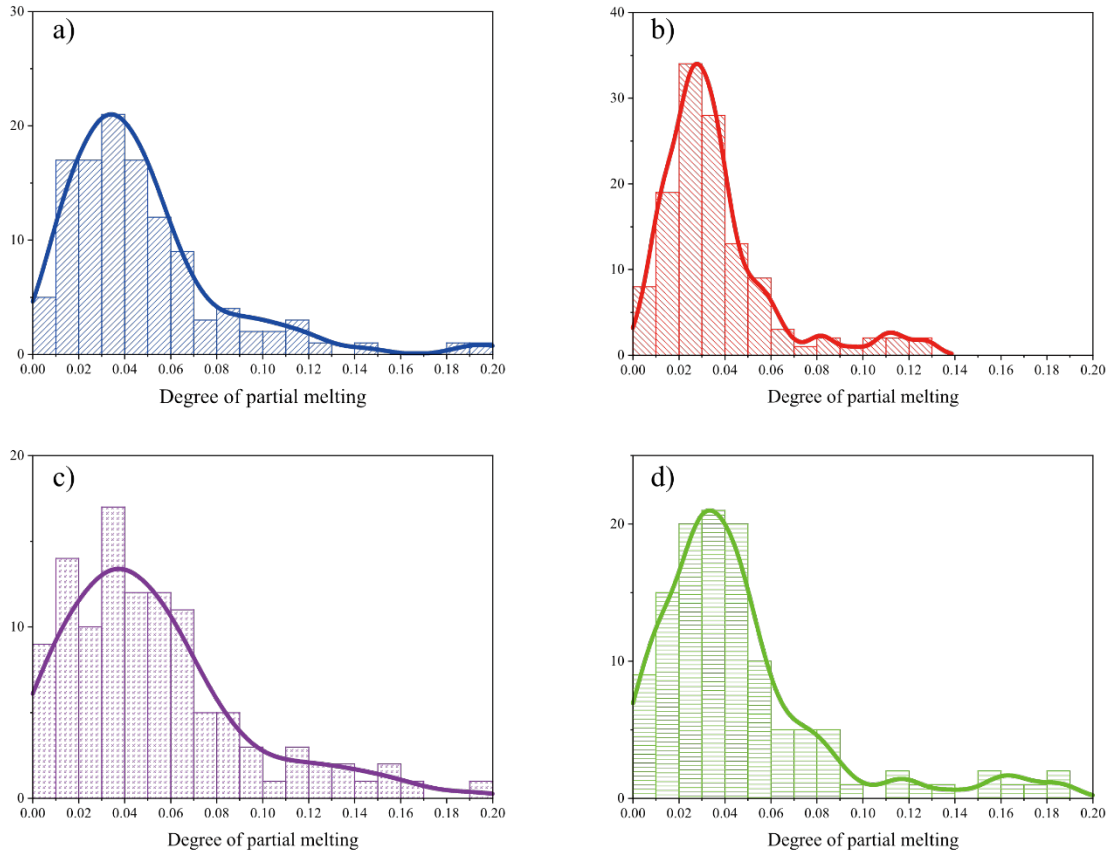


Figure S1. Histograms showing the modeled partial melting degree of the Low-Mg peridotite. a) and c) and b) and d) correspond to batch and fractional partial melting, respectively. The modeling follows the mode of Norman (1998). The initial compositions are assumed to be DMM of Workman and Hart (2005) and PM of McDonough and Sun (1995) for batch and fractional melting modeling, respectively.

Table S1. Modal abundance of Ol, Opx, Cpx, and Sp and Mg-number of peridotites from the North China Craton

Table S2. Temperature and oxygen fugacity estimations for peridotites from the North China Craton

Table S3. Oxygen fugacity of Kaapvaal, Slave, and Siberia craton

Table S4. Fluids species with oxygen fugacity ranging from ΔFMQ -1 to -4 calculated via GFluids under 950 °C and 1.5 GPa

Table S5. Published water content of peridotite xenoliths from the North China Craton vs. the oxygen fugacity

Table S6. Partial melting degree of Low-Mg peridotites calculated via model proposed by Norman (1989) and assuming the initial composition of DMM of Workman and Hart (2005) and PM of McDonough and Sun (1995)

Table S7. Composition of primary melts derived from pMELTS simulation

Data Set S1. Major element of olivine, orthopyroxene, clinopyroxene, and spinel for each referred peridotite.